Received: 30 December 2022 | Revised: 13 April 2023 | Accepted: 16 May 2023

DOI: 10.1111/ffe.14076

ORIGINAL ARTICLE

FFEMS Fatigue & Fracture of Engineering Materials & Structures WILEY

Secondary orientation effects on the low cycle fatigue behaviors of rectangular-sectional Ni-based single crystal superalloys at medium and high temperatures

Shao-Shi Rui[1] | **Zhiwu He**[2] | **Yiyun Guo**[1,3] | **Yue Su**[4] | **Qi-Nan Han**[5] | **Xianfeng Ma**[6] | **Hui-Ji Shi**[7]

[1]State Key Laboratory of Nonlinear Mechanics (LNM), Institute of Mechanics, Chinese Academy of Sciences, Beijing, China

[2]Anker Innovations Technology Co., Ltd., Shenzhen, Guangdong, China

[3]School of Engineering Science, University of Chinese Academy of Sciences, Beijing, China

[4]School of Power and Energy, Northwestern Polytechnical University, Xi'an, Shaanxi, China

[5]College of Energy and Power Engineering, Nanjing University of Aeronautics and Astronautics, Nanjing, Jiangsu, China

[6]Sino-French Institute of Nuclear Engineering and Technology, Sun Yat-Sen University, Zhuhai, Guangdong, China

[7]Applied Mechanics Laboratory (AML), School of Aerospace Engineering, Tsinghua University, Beijing, China

Correspondence
Prof. Xianfeng Ma, Sino-French Institute of Nuclear Engineering and Technology, Sun Yat-Sen University, Zhuhai, Guangdong 519082, China.
Email: maxf6@mail.sysu.edu.cn

Prof. Hui-Ji Shi, Room N-513, Mong Man Wai Building of Science and Technology, Tsinghua University, Beijing 100084, China.
Email: shihj@mail.tsinghua.edu.cn

Funding information
National Natural Science Foundation of China, Grant/Award Numbers: 12002155, 12102348, 12172193, 12202446, U2032143; Opening Fund of State Key Laboratory of Nonlinear Mechanics; National Major Science and Technology Projects of China, Grant/Award Number: J2019-VI-0002-0115; Opening Fund of Key Laboratory of Aero-engine Thermal Environment and Structure; Ministry of Industry and Information Technology, Grant/Award Number: CEPE2022004

Abstract

Turbine blades made of Ni-based single crystal superalloys (NBSXs) have long-strip shaped cross sections and rectangular-sectional structures, where the secondary orientation produces potential effects even the primary orientation is fixed at [001]. Low cycle fatigue behaviors between [010] and [110] transversely oriented rectangular-sectional NBSX specimens were compared. Obvious differences existed under 600°C but disappeared under 850°C, with the deformation mechanism and fracture mode transitions. Secondary orientation effects on stress asymmetry and fatigue life cannot be described by the conventional LCP model and critical plane method but were well explained by dislocation path length-dependent back-stress model and A.N. May's random slip model.

KEYWORDS

fatigue life, low cycle fatigue, NBSXs, secondary orientation effects, stress asymmetry

Highlights

- Secondary orientation effects on rectangular-sectional NBSXs under 600°C are more obvious than those under 850°C;
- [110] case shows higher stress asymmetry and longer fatigue life than [010] case under 600°C;
- The secondary orientation effect on stress asymmetry is attributed to the different dislocations paths;

- The secondary orientation effect on fatigue life is attributed to the different dislocations intrusions' depths.

1 | INTRODUCTION

γ' (Ni_3Al) precipitation-hardened Ni-based single crystal superalloys (NBSXs), such as the PWA1483/1484, CMSX-3/4, and DD5/6, are typical high-temperature materials widely employed for turbine blades of aero-engines or gas turbines.[1] They have excellent fatigue properties when subjected to cyclic loading under medium and high temperatures, especially along the crystal orientation [001]. In view of the repeated start/stop operations on aero-engines or gas turbines, low cycle fatigue has become one of the major failure types in those turbine blades. It has been known to all that the primary orientation (i.e. the crystallographic orientation along the loading direction) will produce a strong influence on the low cycle fatigue behaviors due to the anisotropy of face-centered cubic (FCC) lattice structure.[2] When the primary orientation is changed, the activated slip factors in {111} < 101 > octahedral slip system, as well as their spatial relationships with respect to the geometric profiles of round bar specimens will also be different, and therefore the low cycle fatigue behaviors of NBSXs are then influenced. A widely accepted view is that the primary orientation should be fixed at [001] in the turbine blades because the resistance to fatigue failure along that crystal orientation is the best.

Tension-compression stress asymmetry is the most unique low-cycle fatigue behavior in NBSXs[3] compared to other common structural alloys. This phenomenon is firstly reported in Ni_3(Al, Nb)[4] or Ni_3Ga[5] single crystal intermetallic compounds with LI_2 lattice structure, and then extended to other γ' precipitation-hardened NBSXs,[6–10] whose causation was usually attributed to the so called "Non-Schmid" yield behavior.[11–13] Our co-authors X. Ma and H.-J. Shi[14] compared the low cycle fatigue behaviors of PWA1483 NBSXs under medium temperature (MT, 600°C) and high temperature (HT, 850°C) in the previous research, and their results indicated that the stress asymmetry is very obvious under MT but gradually weakened when the temperature increases to HT, accompanied by a fracture mode transition from the "crystallographic type" to the "non-crystallographic type". The stress asymmetry behavior of NBSXs shows both the primary orientation and the temperature dependence, which can be explained by the conventional LCP model[15] considering the cross slip of dislocations.

Fatigue failure is another common but very important low-cycle fatigue behavior in NBSXs, and the related fatigue life of NBSXs under certain test conditions (strain amplitude, temperature, etc.) is a key parameter indicating their resistance to fatigue failure. The low cycle fatigue crack nucleation in NBSXs is achieved by the formation of Persistent Slip Band (PSB) under $T < 760 \sim 800°C$,[16–18] where the micro notches accumulated by intrusions of those dislocations escaping from wall surfaces can induce stress concentration and then serve as the fatigue crack sources. Different from fatigue lives of those isotropic materials following the conventional Manson-Coffin's law,[19,20] the fatigue life of anisotropic NBSXs shows strong primary orientation dependence, which can be predicted by the critical plane method.[21–28] The activated {111} slip planes of NBSXs are usually defined as the critical planes[25] because the fatigue cracks usually nucleate along these planes under the crystallographic fracture mode. The critical plane parameters are the algebraic combinations of normal/shear strain amplitude, maximum normal/shear strain, normal/shear stress amplitude, as well as maximum normal/shear stress on critical planes, which uniquely depend on the selection of primary orientation.

For those isotropic-sectional structures like a round bar subjected to uniaxial loading, the primary orientation along the lengthwise direction is the only one factor influencing the mechanical behaviors of NBSXs. With the same primary orientation, the resolved shear stress of each slip factor and the critical plane parameters on {111} slip planes have already been determined, and so are the low cycle fatigue behaviors. However, the actual structures of turbine blades are not always isotropic-sectional, and they usually have long-strip-shaped or rectangular-sectional cross-sections. In that case, the secondary orientation along the transverse direction of turbine blades becomes another potential factor in addition to the primary orientation, which also turns out to produce significant effects on the selection of the activated slip plane[29] even if the primary orientation has already been fixed at [001]. That phenomenon is unexplainable under the framework of LCP model

and critical plane method, because the introduction of secondary orientation into NBSXs by changing the shape of cross-section cannot directly change the resolved shear stresses and critical plane parameters, and thus should not produce any extra effects on the low cycle fatigue behaviors of NBSXs subjected to uniaxial loading.

Neither the LCP model nor the critical plane method take the secondary orientation effects into consideration, and thus neither the tension-compression stress asymmetry difference nor the fatigue life difference between [010] and [110] transversely oriented rectangular-sectional specimens can be well explained under the current theoretical framework. The motivation behind this research is to reveal the secondary orientation effects on low cycle fatigue behaviors of NBSXs subjected to symmetric cyclic deformation (strain ratio $R_\varepsilon = -1$) along the primary orientation [001] under MT (600°C) and HT (850°C), especially to understand the changes of tension-compression stress asymmetry and low cycle fatigue life when the secondary orientation is changed from [010] to [110]. For that purpose, low cycle fatigue tests by specially designed rectangular-sectional specimens were conducted, whose differences between two different secondary orientations can be well explained by the dislocation path length dependent back-stress model and the A.N. May's random slip model.[30,31]

2 | MATERIAL AND METHODS

2.1 | Material

The material used for low cycle fatigue tests in this research is PWA1483, a kind of the 1st generation NBSXs produced by Pratt & Whitney Group, Co., Ltd., USA. They are widely employed at the hot-end turbine blades of gas turbines, and their chemical components are shown in Table 1. The dimension of the as-received NBSX bar is 235 mm × 110 mm × 20 mm, the nominal primary orientation along its lengthwise direction (i.e. the solidification direction) is [001], and the nominal secondary orientations along its transverse and normal directions are [010] and [100] respectively.

Rotating Orientation X-Ray Diffraction (RO-XRD)[32] measurement was further conducted, in which test the NBSX bar is fixed on a rotating table attached to the instrument while the detector is set at the diffraction angle $2\theta_0$. While the bar specimen is θ-scanning (between 0 and $2\theta_0$), it rotates at a fairly high speed around the normal axis of the specimen surface. In this process, there will be some crystal planes whose deviation angles $\emptyset$ from the surface plane are between 0 and $2\theta_0$, so that their normal axes cross the horizontal plane twice. When that happens, the diffraction ray must be in the horizontal plane, the θ-scanning offsets the deviation angle $\emptyset$, and the detector at $2\theta_0$ may receive reflected X-Rays. The detailed information of those crystal planes having different deviation angles $\emptyset$ may be then displayed in the scanning diagrams. If two peak positions of the scanning curve are θ_1 and θ_2 which can be captured directly in the scanning diagram, then the spatial deviation angles $\emptyset = 0.5\ (\theta_1 - \theta_2)$ between the specific crystal plane and the surface plane are obtained to help determine the crystal plane parallel to the specimen surface. The measurement results confirmed that all the deviations between nominal orientations and true orientations along three directions are within 5°. A 5° deviation is small enough to be ignored because the maximum Schmid Factor of the octahedral slip systems $\{111\} < 110 >$ will not be changed obviously (no more than 8%) if such a deviation exists.

The microstructures of NBSXs are made up of two different phases: the γ (Ni, FCC) matrix and the cubic γ' (Ni_3Al, LI_2) precipitations with scales of several hundred nanometers, between which the lattice coherent relationship exists, as shown in Figure 1A. The γ' precipitations of high volume fraction can provide the precipitation strengthening effect on NBSXs. According to the previous research on another similar directionally solidified Ni-based superalloys reported by our co-authors Z. He and H.-J. Shi,[33] the plastic deformation of NBSXs is achieved by the planar slip along $\{111\} < 101 >$ octahedral slip system primarily, then the cross slips along $\{010\} < 101 >$ cubic slip system secondarily under MT (600°C), and further coupled with dislocations climb under HT (850°C), as shown in Figure 1B.

As a natural result of plastic deformation mechanisms transition from MT to HT, the low cycle fatigue fracture modes will also be different under the above two temperatures, as revealed by our co-authors Z. He et al.[33] In the former case, these mobile dislocations will cut the γ matrix and γ' precipitations together, thus induce the crystallographic fracture along activated {111} slip planes. By contrast, in the latter case, they only slip or climb

Elements	Cr	Co	Mo	Al	Ti	Ta	W	C	Ni
wt.%	12.2	9.0	1.9	3.6	4.1	5.0	3.8	0.07	Bal.

TABLE 1 The chemical components of NBSXs are used in this research.

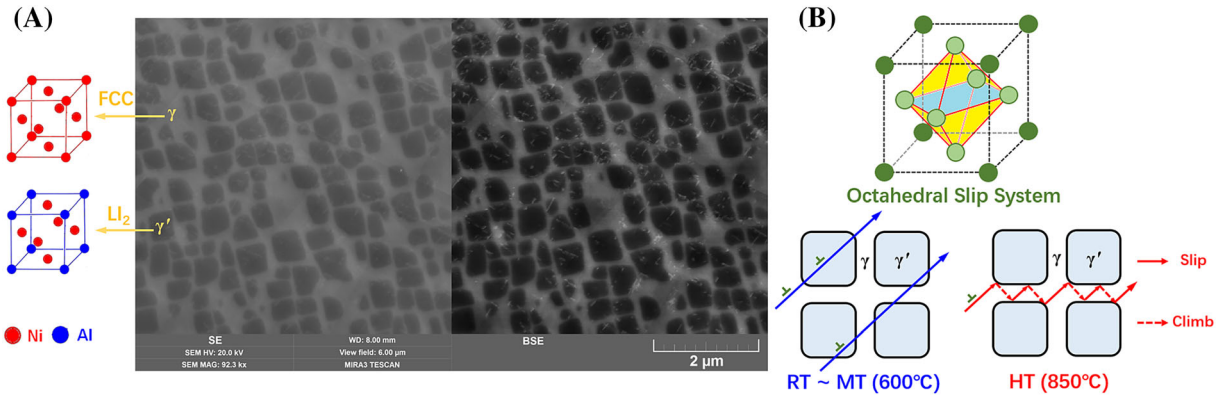

FIGURE 1 (A) The microstructures and (B) the plastic deformation mechanisms of NBSXs. [Colour figure can be viewed at wileyonlinelibrary.com]

inside the γ matrix but bypass the γ' precipitations, thus will cause the non-crystallographic fracture along the plane perpendicular to the loading direction.

2.2 | Method

According to ASTM E606–04,[34] the standard round bar specimen with threaded end connection is more recommended for strain-controlled low cycle fatigue test, but its cylinder cross section cannot achieve different secondary orientations. And as an alternative one, the plate specimen with rectangular cross-section cannot achieve the threaded end connection. Therefore, we design the special specimen in this research, combining the rectangular test section and cylinder end section, to achieve different secondary orientations without changing the threaded end connection. The newly modified specimens for investigating the secondary orientation effects in this research have 22 mm × 12 mm × 4 mm rectangular gauge sections, as shown in Figure 2A. These low-cycle fatigue specimens are taken from a PWA1483 NBSX bar, by the way as shown in Figure 2B. Their loading directions are all parallel to the lengthwise direction of NBSX bar (along the [001] orientation). However, the transverse directions of their rectangular-sectional gauge sections are not the same, one half (① ∼ ③) is parallel to the transverse direction of NBSX bar (along the [010] orientation), while the other half (④∼ ⑥) form a 45° angle with the transverse direction of NBSX bar (along the [110] orientation). The flat parts of all the rectangular-sectional specimens used for low-cycle fatigue tests in this research have already been polished carefully in advance, and thus the surface residual stress can be ignored.

The low cycle fatigue tests were carried out by a type MTS809.2 hydraulic servo fatigue testing machine. The temperature was raised by resistance heating wires, which are controlled based on the feedback from three thermocouples located on the surface of gauge sections, and the accuracy is within ± 1°C. The extensometer length for measuring the applied strain is 12 mm. The tensile and compressive strains were applied symmetrically (strain ratio $R_\varepsilon = -1$) with ± 0.1%/sec strain rate and triangle strain waveform, as shown in Figure 3. No holding stage existed during the whole loading period. The criterion for fatigue failure is a 5% drop of maximum tensile stress under a fixed strain amplitude.

The experimental scheme of low-cycle fatigue tests is given in Table 2. Three strain amplitudes ± 0.63%, ± 0.66%, ± 0.69% are selected for each half of the specimens with secondary orientations [010] and [110], and two temperatures MT (600°C) and HT (850°C) are selected for all the specimens.

3 | RESULTS

3.1 | Results of low cycle fatigue tests on rectangular-sectional specimens under MT and HT

The results of low cycle fatigue tests under MT (600°C) and HT (850°C) on rectangular-sectional NBSX specimens having different secondary orientations [010] and [110] are given here. A typical hysteretic loop of engineering stress–engineering strain and the corresponding evolution curve of stress amplitude subjected to strain amplitude of ± 0.63% under MT (600°C) are shown in Figure 4, from which a significant difference can be noticed. Figure 4(A) indicated that the tension-compression stress asymmetry of [110] transversely oriented specimen is more obvious than that of [010] transversely oriented specimen, though their tensile and

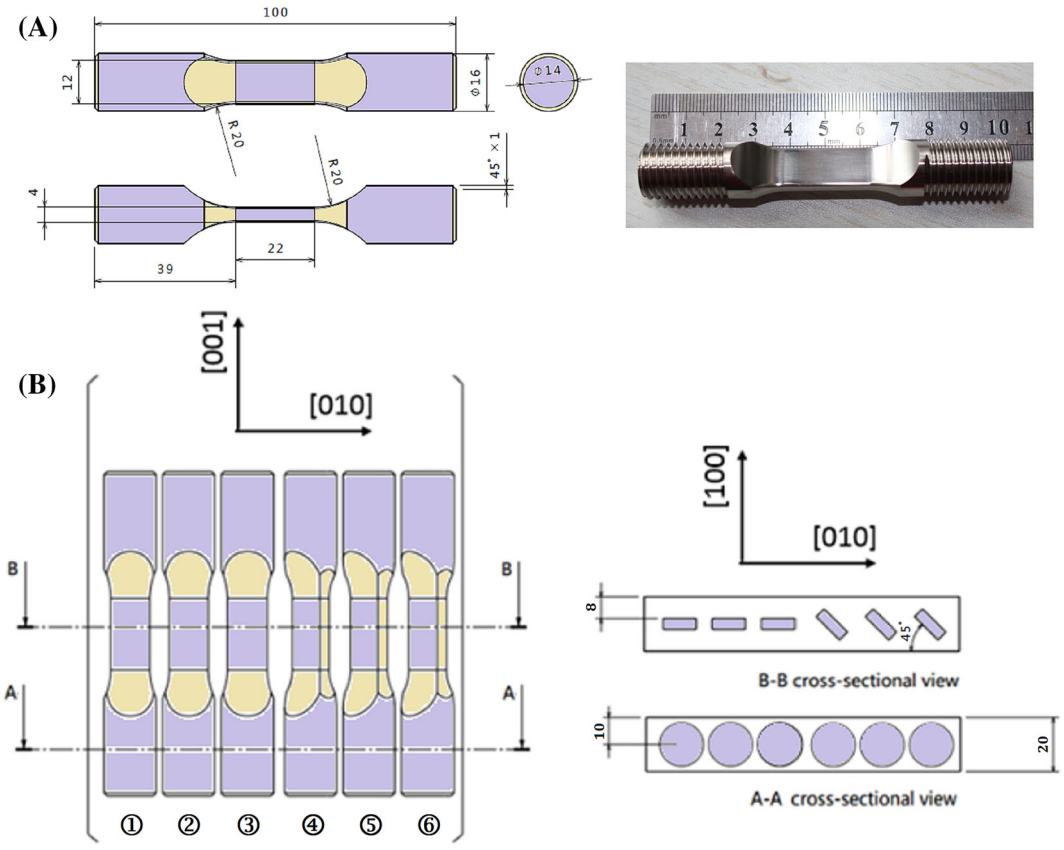

FIGURE 2 The way of taking rectangular-sectional low cycle fatigue specimens from the PWA1483 NBSX bar. [Colour figure can be viewed at wileyonlinelibrary.com]

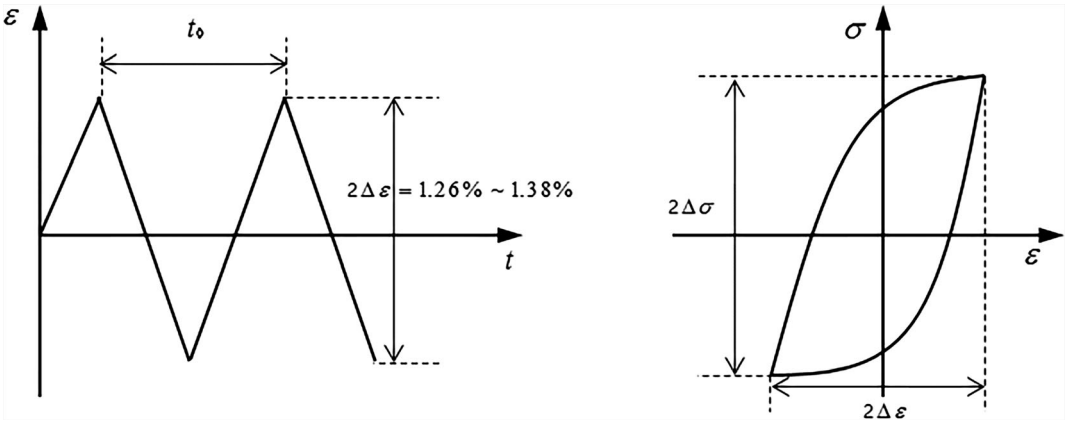

FIGURE 3 The triangle strain waveform and the stress—strain hysteretic loop.

TABLE 2 The experimental scheme of low cycle fatigue tests on PWA 1483 NBSX specimens.

Secondary orientation	[010]			[110]		
Specimen number	①	②	③	④	⑤	⑥
Strain Amplitude	± 0.63%	± 0.66%	± 0.69%	± 0.63%	± 0.66%	± 0.69%
Test Temperature	MT (600°C) and HT (850°C)					

compressive strains are completely symmetric. Figure 4 (B) indicated that the stress amplitude of [110] transversely oriented specimen is lower than that of [010] transversely oriented specimen, though their strain amplitudes ± 0.63% are the same. It is a bit amazing that the secondary orientations difference ([010] vs. [110]) can produce such a significant effect on the cyclic deformation behaviors of rectangular-sectional specimens, even if their primary orientations have been fixed at [001]. Also, compared to those round bar NBSX specimens without secondary orientation features, the existence of wall surface along specified secondary orientation indeed affects the fatigue behaviors of rectangular-sectional NBSX specimens.

The comparison of stress ratios (the ratio between maximum tensile stress and maximum compressive stress) between standard round bar specimens (black data points "Standard") and rectangular-sectional specimens (blue data points "[010]" vs. red data points "[110]") under 600°C and 850°C are shown in Figure 5. Therein the data points of rectangular-sectional specimens with different secondary orientations are given by low cycle fatigue tests in this research, and those of round standard bar specimens (∅ 8 mm) come from our previous work by co-authors X. Ma et al.[14]

Under MT (600°C), the tensile stress is greater than the compressive stress ($R_\sigma > 1$) when the strain amplitude ranges from ± 0.57% to ± 0.82%. In addition, the

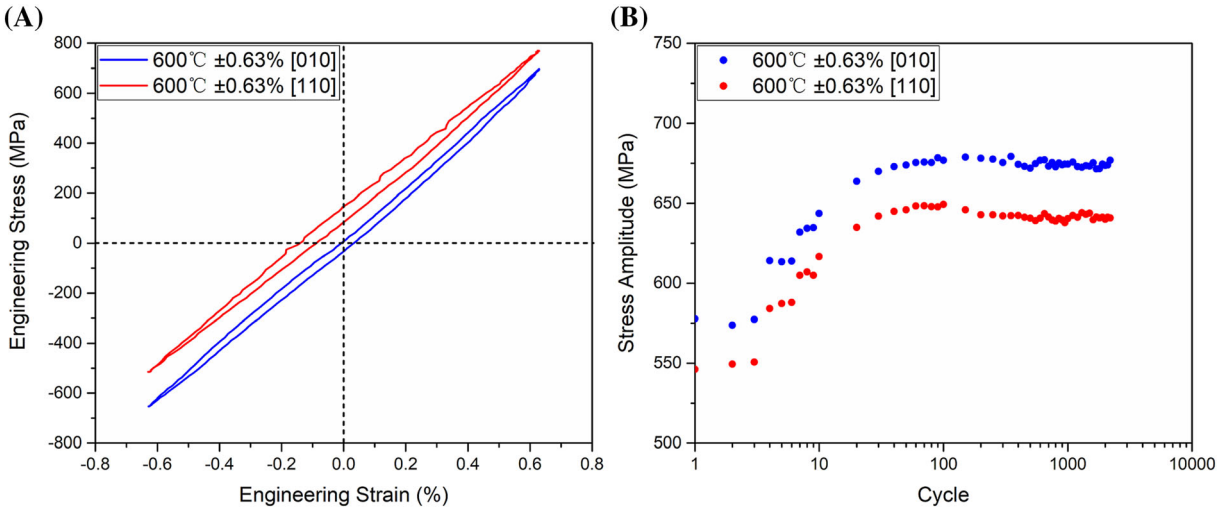

FIGURE 4 (A) Hysteretic loop and (B) stress amplitude evolution subjected to ± 0.63% under 600°C. [Colour figure can be viewed at wileyonlinelibrary.com]

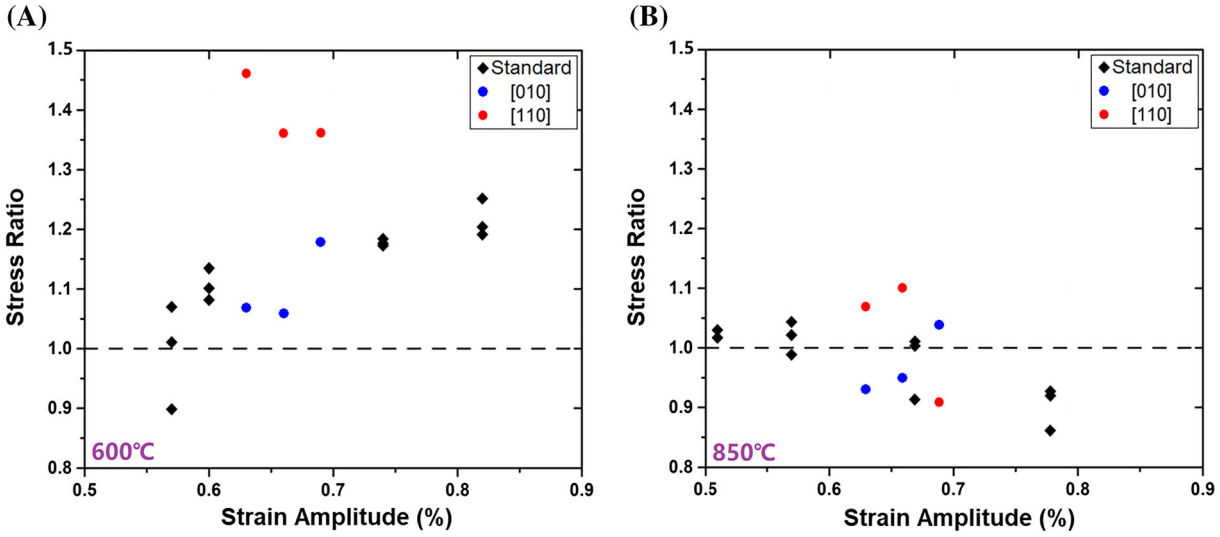

FIGURE 5 Stress ratios of standard round bar specimens (black data points "standard") and different rectangular-sectional specimens (blue data points "[010]" vs. red data points "[110]") under (A) 600°C and (B) 850°C. [Colour figure can be viewed at wileyonlinelibrary.com]

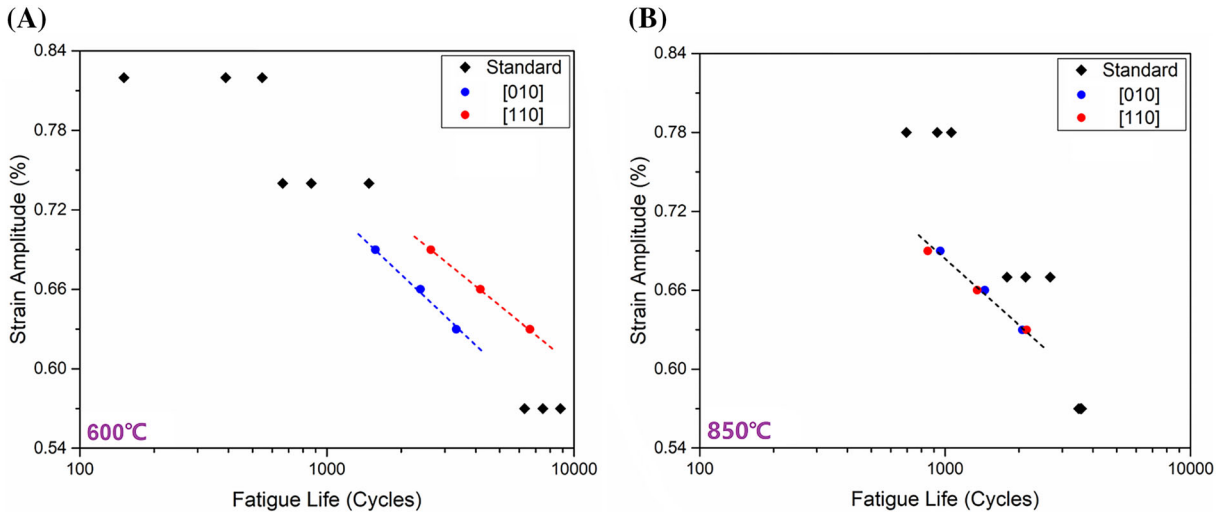

FIGURE 6 *S*-N_f curves of standard round bar specimens (black data points "standard") and different rectangular-sectional specimens (blue data points "[010]" vs. red data points "[110]") under (A) 600°C and (B) 850°C. [Colour figure can be viewed at wileyonlinelibrary.com]

blue data points of [010] transversely oriented rectangular-sectional specimens agree with the tendency of those black data points of standard round bar specimens, while the red data points of [110] transversely oriented rectangular-sectional specimens deviate from that tendency obviously, and become much larger than black and blue data points. The stress asymmetry of rectangular-sectional specimen depends on the secondary orientation under the MT, where that of [110] case is more obvious than that of [010] case.

Under HT (850°C), the tensile stress becomes very close to the compressive stress ($R_\sigma \approx 1$) when the strain amplitude ranges from ± 0.51% to ± 0.78%. Both the blue data points and the red data points of [010] and [110] transversely oriented rectangular-sectional specimens respectively agree with the tendency of those black data points of standard round bar specimens. The stress asymmetry of rectangular-sectional specimen becomes no longer secondary orientation dependent under the HT.

Figure 6 gives the low cycle fatigue life versus the strain amplitude (*S*-N_f curves, $S = \Delta\varepsilon$) of standard round bar specimens (black data points) and rectangular-sectional specimens (blue data points [010] vs. red data points [110]) under MT (600°C) and HT (850°C). Both the blue data points and the red data points are located within the scatter band of those black data points, following the power law (i.e. the linear relationship under logarithmic coordinate), since all the specimens have the same primary orientation [001]. Under MT (600°C), the fatigue life of [110] case is much longer than that of [010] case at the same strain amplitude, and two different lines are necessary to fit the blue and red data points respectively, as shown in Figure 6A, where the fatigue life depends on the secondary orientation of rectangular-sectional specimen. On the contrary, under HT (850°C), the fatigue life of [110] case is close to that of [010] case at the same strain amplitude, and only one single line is enough to fit both the blue data points and red data points at the same time, as shown in Figure 6B, where the fatigue life in each case no longer depends on the secondary orientation of rectangular-sectional specimen.

All the cyclic stress data of stable hysteretic loops at the middle life cycle ($N_f/2$), including the stress amplitude, stress upper, stress lower, stress mean, and stress ratio, as well as the corresponding fatigue life cycles (N_f) subjected to different temperatures (600°C vs. 850°C), secondary orientations ([010] vs. [110]) and strain amplitudes (± 0.63%, ± 0.66%, ± 0.69%), have been listed in Table 3.

3.2 | Fractographs of rectangular-sectional specimens after fatigue fracture under MT and HT

Figure 7 gives the fractographs of rectangular-sectional specimens with different secondary orientations ([010] vs. [110]) after fatigue fracture under MT (600°C) and HT (850°C). It can be seen clearly that the fracture surface topography fluctuation under MT (600°C) is more obvious than that under HT (850°C). The former consists of various smooth facets having a certain angle to the loading direction, and the latter is a whole rough plane perpendicular to the loading direction (Mode I fracture). The above fractographs difference of rectangular-sectional specimens between MT and HT revealed the transition between two fracture modes: the "crystallographic

TABLE 3 The cyclic stress (unit: MPa) of stable hysteretic loops and the corresponding fatigue life.

Temperature	Secondary orientation	Strain amplitude	Stress amplitude	Stress upper	Stress lower	Stress mean	Stress ratio	Fatigue life
600°C	[010]	± 0.63%	± 675	697	−653	22	1.07	3,336
		± 0.66%	± 659	677	−641	18	1.06	2,394
		± 0.69%	± 717	776	−658	59	1.18	1,573
	[110]	± 0.63%	± 640	759	−521	119	1.46	6,631
		± 0.66%	± 632	729	−535	97	1.36	4,183
		± 0.69%	± 667	769	−565	102	1.36	2,636
850°C	[010]	± 0.63%	± 582	561	−603	−21	0.93	2064
		± 0.66%	± 600	586	−614	−14	0.95	1,452
		± 0.69%	± 590	602	−578	12	1.04	956
	[110]	± 0.63%	± 566	584	−548	18	1.07	2,148
		± 0.66%	± 568	594	−542	26	1.10	1,350
		± 0.69%	± 581	553	−609	−28	0.91	850

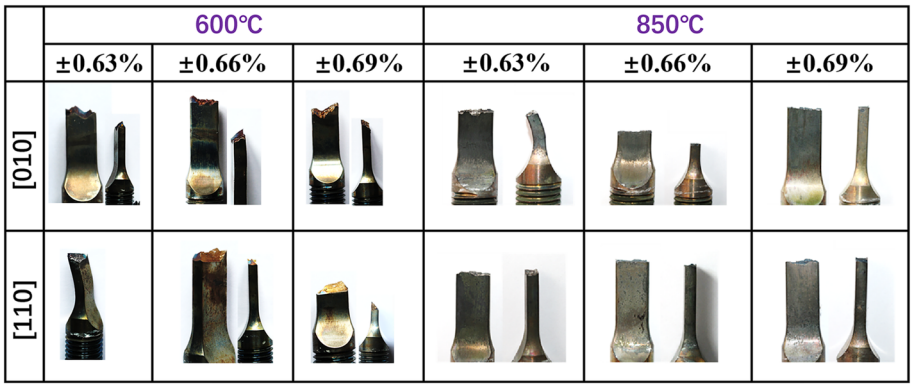

FIGURE 7 Fractographs of different rectangular-sectional specimens with different secondary orientations ([010] vs. [110]) under 600°C and 850°C. [Colour figure can be viewed at wileyonlinelibrary.com]

fracture mode" and the "non-crystallographic fracture mode", which coincides with the transition of plastic deformation mechanisms from MT (600°C) to HT (850°C), as mentioned in the above *section 2.1*. In particular, this transition exists in not only NBSXs but also directionally solidified Ni-based superalloys according to the previous research by our co-authors Z. He and H.-J. Shi.[33] Some specimens present buckling after failure, but we concluded that such buckling only developed during the very last cycles when a crack was propagating rapidly because the loading and unloading of Young's moduli of the stable hysteretic loop are the same in the middle life. So, the above fatigue test results are still reliable.

Figure 8 gives the comparison between two fractographs of rectangular-sectional specimens with different secondary orientations [010] and [110] under MT (600°C). It can be recognized that all fatigue cracks nucleated on wall surfaces. In [010] case those differently oriented facets formed a "V-type" fracture surface, while in [110] case those consistently oriented facets formed a typical shear fracture surface. Scanning Electron Microscope (SEM) observation confirmed that those smooth facets in the fracture surfaces are actually {111} crystal plane clusters as shown in Figure 8A and B, whose spatial configurations in B, whose spatial configurations in the specimen coordinate (lengthwise× transverse × normal) are shown in Figure 8C. Those differently oriented facets in [010] case correspond to two different crystal planes $(1\bar{1}\bar{1})$ and $(11\bar{1})$, while those consistently oriented facets correspond to the same crystal plane $(1\bar{1}1)$.

4 | DISCUSSIONS

For the convenience of discussing the differences between tension-compression stress asymmetry (*Section 4.1*) and low cycle fatigue life (*Section 4.2*) between [010] and [110] transversely oriented rectangular-sectional specimens, it is necessary to establish a coordinate system to describe the spatial configurations of the activated slip

factors subjected to uniaxial loading, named after $S_I\left(\vec{b}_4,\vec{b}_1\right)$, $S_{II}\left(\vec{b}_1,\vec{b}_2\right)$, $S_{III}\left(\vec{b}_2,\vec{b}_3\right)$ and $S_{IV}\left(\vec{b}_3,\vec{b}_4\right)$ respectively, as shown in Figure 9. Therein $\vec{b}$ is the Burgers vector along slip direction, and S is the slip plane of each activated slip factor. In the [010] case, the spatial configurations of four slip factors are equivalent: $S_I\vec{b}_1 = S_{II}\vec{b}_2 = S_{III}\vec{b}_3 = S_{IV}\vec{b}_4$, so are the spatial configurations of other four slip factors: $S_I\vec{b}_4 = S_{II}\vec{b}_1 = S_{III}\vec{b}_2 = S_{IV}\vec{b}_3$, as shown in Figure 9A. In the [110] case, the four slip factors $S_I\vec{b}_1 = S_I\vec{b}_4 = S_{III}\vec{b}_2 = S_{IV}\vec{b}_3$ have the equivalent spatial configurations, so do the other four slip factors $S_{II}\vec{b}_1 = S_{II}\vec{b}_2 = S_{IV}\vec{b}_3 = S_{IV}\vec{b}_4$, as shown in Figure 9B.

Given $\vec{e}_1=[100]$, $\vec{e}_2=[010]$ and $\vec{e}_3=[001]$, then the Burgers vectors $\vec{b}_1=a[011]/2$, $\vec{b}_2=a[101]/2$, $\vec{b}_3=a[0\bar{1}1]/2$ and $\vec{b}_4=a[\bar{1}01]/2$ of the slip factors can be expressed as Equation (1):

$$\vec{b}_1=\frac{a}{2}\left(\vec{e}_2+\vec{e}_3\right),\ \vec{b}_2=\frac{a}{2}\left(\vec{e}_1+\vec{e}_3\right),\ \vec{b}_3=\frac{a}{2}\left(-\vec{e}_2+\vec{e}_3\right),\ \vec{b}_4=\frac{a}{2}\left(-\vec{e}_1+\vec{e}_3\right) \tag{1}$$

At the same time, the spacing vectors $\vec{n}_I$, $\vec{n}_{II}$, $\vec{n}_{III}$ and $\vec{n}_{IV}$ along the normal directions of four activated slip

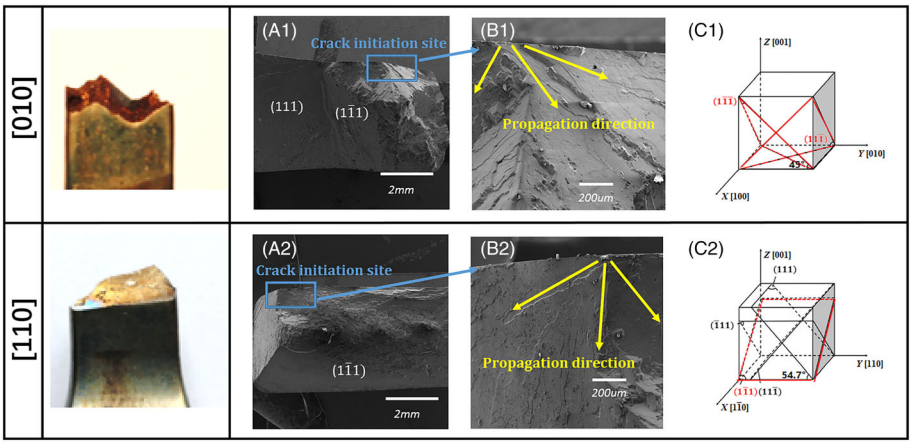

FIGURE 8 Comparison between two fractographs of rectangular-sectional specimens with different secondary orientations ([010] vs. [110]) under 600°C: (A) the crack initiation site, (B) the crack propagation direction, and (C) the cleavage crystal planes along the activated slip planes {111}. [Colour figure can be viewed at wileyonlinelibrary.com]

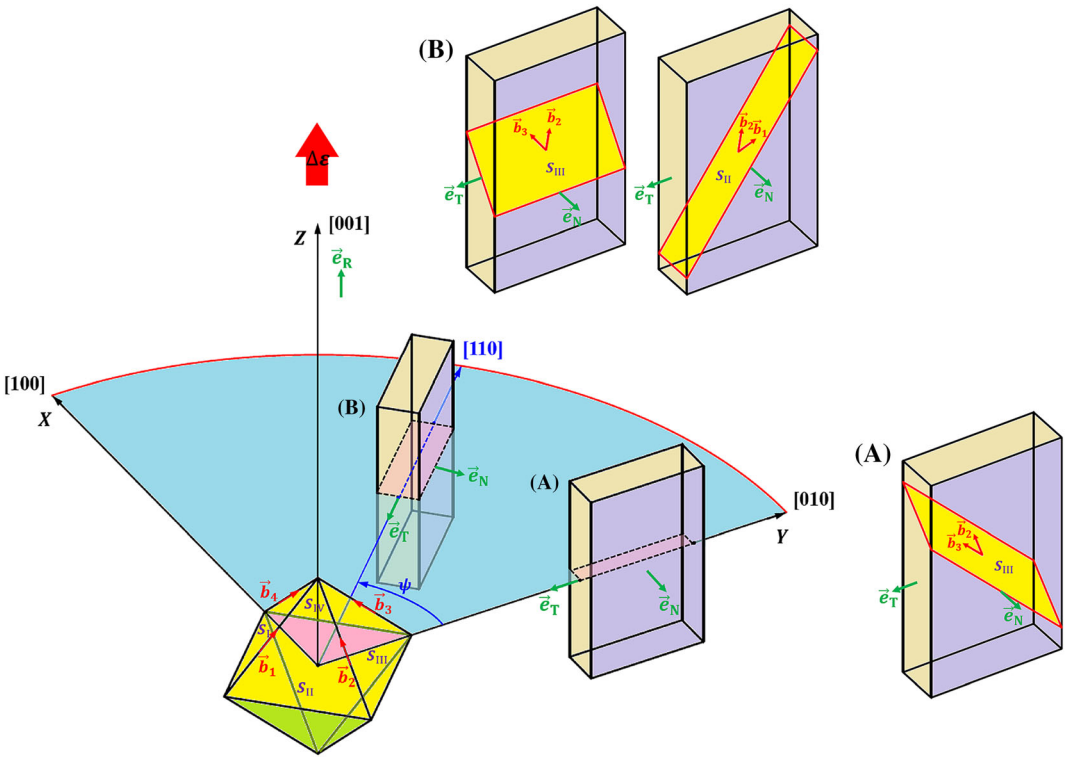

FIGURE 9 The activated slip factors in (A) [010] and (B) [110] transversely oriented rectangular-sectional specimens. [Colour figure can be viewed at wileyonlinelibrary.com]

planes $\boldsymbol{S}_{\mathrm{I}}=(1\bar{1}1)$, $\boldsymbol{S}_{\mathrm{II}}=(\bar{1}\bar{1}1)$, $\boldsymbol{S}_{\mathrm{III}}=(\bar{1}11)$ and $\boldsymbol{S}_{\mathrm{IV}}=(111)$ are shown in Equation (2):

$$\vec{\boldsymbol{n}}_{\mathrm{I}}=\frac{a}{3}\left(\vec{\boldsymbol{e}}_1-\vec{\boldsymbol{e}}_2+\vec{\boldsymbol{e}}_3\right),\ \vec{\boldsymbol{n}}_{\mathrm{II}}=\frac{a}{3}\left(-\vec{\boldsymbol{e}}_1-\vec{\boldsymbol{e}}_2+\vec{\boldsymbol{e}}_3\right),\ \vec{\boldsymbol{n}}_{\mathrm{III}}=\frac{a}{3}\left(-\vec{\boldsymbol{e}}_1+\vec{\boldsymbol{e}}_2+\vec{\boldsymbol{e}}_3\right),\ \vec{\boldsymbol{n}}_{\mathrm{IV}}=\frac{a}{3}\left(\vec{\boldsymbol{e}}_1+\vec{\boldsymbol{e}}_2+\vec{\boldsymbol{e}}_3\right) \tag{2}$$

The lengthwise direction $\vec{\boldsymbol{e}}_{\mathrm{R}}$, the transverse direction $\vec{\boldsymbol{e}}_{\mathrm{T}}$ and the normal direction $\vec{\boldsymbol{e}}_{\mathrm{N}}$ of rectangular-sectional specimens can be expressed as Equation (3). ψ is the angle between the transverse direction $\vec{\boldsymbol{e}}_{\mathrm{T}}$ and the [010] orientation $\vec{\boldsymbol{e}}_2$, where $\psi=0°$ and 45° when the secondary orientation is [010] and [110].

$$\vec{\boldsymbol{e}}_{\mathrm{R}}=\vec{\boldsymbol{e}}_3,\ \vec{\boldsymbol{e}}_{\mathrm{T}}=-\sin\psi\,\vec{\boldsymbol{e}}_1-\cos\psi\,\vec{\boldsymbol{e}}_2,\ \vec{\boldsymbol{e}}_{\mathrm{N}}=-\cos\psi\,\vec{\boldsymbol{e}}_1+\sin\psi\,\vec{\boldsymbol{e}}_2 \tag{3}$$

4.1 | Stress asymmetry difference between [010] and [110] transversely oriented specimens

The tension-compression stress asymmetry phenomenon in pure Ni_3Al single crystal or NBSXs with γ' (Ni_3Al) precipitations has been noticed for quite a long time, which cannot be explained by the conventional Schmid's law[35] and thus be called "Non-Schmid effect".[11–13] A suitable explanation to the stress asymmetry phenomenon in NBSXs is the LCP model developed by C. Lall, S. Chin, and D.P. Pope[15] in 1979. The LCP model assumes that the yield behaviors of NBSXs are controlled by not only the resolved shear stress applied in the {111} < 101 > octahedral slip system primarily, but also the resolved shear stress applied in the {010} < 101 > cubic slip system secondarily, which two resolved shear stresses constitute the former two items together in a modified yield criterion Equation (4):

$$\tau^{*}=\overbrace{\bar{\tau}_{(111)[\bar{1}01]}}^{\text{Schmid item}}+\overbrace{\mu\tau_{(010)[\bar{1}01]}+\underbrace{\lambda\boldsymbol{\delta}(\sigma_{\mathrm{r}})\tau_{(111)[1\bar{2}1]}}_{\text{Stress asymmetry item}}}^{\text{Non-Schmid item}} \tag{4}$$

In particular, the cores of a < 101>/2 screw dislocations on the {111} octahedral slip planes are initially dissociated and must be constricted before they can cross slip into the {010} cubic slip planes, which is the well-known "core width effect"[12] influencing their cross slip behaviors. The $a[\bar{1}01]/2$ dislocation core is constricted by a resolved shear stress applied in the (111) $[1\bar{2}1]$ under compression, push the partial dislocations $a[\bar{1}\bar{1}2]/6$ and $a[\bar{2}11]/6$ together and promoting the cross slip. Instead, the $a[\bar{1}01]/2$ dislocation core will be extended by a resolved shear stress applied in the (111) $[1\bar{2}1]$ under tension, pull the partial dislocations $a[\bar{1}\bar{1}2]/6$ and $a[\bar{2}11]/6$ apart and retarding the cross slip. The item reflecting the core width effect and causing the tension-compression stress asymmetry is written as the third part in the above yield criterion, and then the yield strength $\sigma_{\mathrm{r}}^{\mathrm{YS}}$ can be expressed as Equation (5):

$$\sigma_{\mathrm{r}}^{\mathrm{YS}}=\frac{\tau^{*}}{\mathrm{SF}_{(111)[\bar{1}01]}+\mu\mathrm{SF}_{(010)[\bar{1}01]}+\lambda\boldsymbol{\delta}(\sigma_{\mathrm{r}})\mathrm{SF}_{(111)[1\bar{2}1]}} \tag{5}$$

The $\mathrm{SF}_{(111)[\bar{1}01]}$, $\mathrm{SF}_{(010)[\bar{1}01]}$ and $\mathrm{SF}_{(111)[1\bar{2}1]}$ are SF values of slip factors (111) $[\bar{1}01]$, (010) $[\bar{1}01]$, and (111) $[1\bar{2}1]$ subjected to the uniaxial loading along [001]. τ^{*}, μ, and λ are temperature-dependent material constants. $\boldsymbol{\delta}(\sigma_{\mathrm{r}})$ is the stress sign, which is equal to 1 in the tensile case ($\sigma_{\mathrm{r}}>0$) and −1 in the compressive case ($\sigma_{\mathrm{r}}<0$), and the sign change of $\boldsymbol{\delta}(\sigma_{\mathrm{r}})$ is the major reason for stress asymmetry.

However, the LCP model can only explain the dependence of tension-compression stress asymmetry on the primary orientation, because those SF values in Equation (5) only depend on the primary orientation, but have nothing to do with the secondary orientation. These SF values are determined when the primary orientation is fixed at [001]: $\mathrm{SF}_{(111)[\bar{1}01]}=1/\sqrt{6}$, $\mathrm{SF}_{(010)[\bar{1}01]}=0$ and $\mathrm{SF}_{(111)[1\bar{2}1]}=\sqrt{2}/6$, whether the secondary orientation is set as [010] or [110]. In addition, the {010} < 101 > cubic slip system cannot be activated, because the $\mathrm{SF}_{\{010\}\langle 101\rangle}$ values are all equal to 0.

To explain the tension-compression stress asymmetry dependent on the secondary orientation, an alternative way is to introduce an average back-stress $\bar{\tau}_{\mathrm{b}}$ in the activated {111} < 101 > slip system, which can weaken the resolved shear stress $\tau_{\{111\}\langle 101\rangle}$ in the tensile case ($\sigma_{\mathrm{r}}>0$) but enhance the resolved shear stress in the compressive case ($\sigma_{\mathrm{r}}<0$). Then the yield criterion for NBSXs is shown in Equation (6):

$$\tau^{*}=\tau_{\{111\}\langle 101\rangle}-\boldsymbol{\delta}(\sigma_{\mathrm{r}})\bar{\tau}_{\mathrm{b}}(L),\ \sigma_{\mathrm{r}}^{\mathrm{YS}}=\frac{\tau^{*}+\boldsymbol{\delta}(\sigma_{\mathrm{r}})\bar{\tau}_{\mathrm{b}}(L)}{\mathrm{SF}_{\{111\}\langle 101\rangle}},\ \sigma_{\mathrm{r}+}^{\mathrm{YS}}-\sigma_{\mathrm{r}-}^{\mathrm{YS}}=\frac{2\bar{\tau}_{\mathrm{b}}(L)}{\mathrm{SF}_{\{111\}\langle 101\rangle}} \tag{6}$$

Therein the average back-stress $\bar{\tau}_{\mathrm{b}}$ should be secondary orientation dependent. In a deeper underlying mechanism reported by literatures, $\bar{\tau}_{\mathrm{b}}$ actually relies on the L (the length of dislocation path moving along the slip

direction across the thickness), and L further relies on the secondary orientation in a rectangular-sectional specimen. As revealed by J.T. Fourie[36–39] and H. Mughrabi,[40–42] the back-stress τ_b is not a constant along the dislocation path after plastic deformation, which is close to zero near the surface but gradually increases to a saturated value $\tau^\dagger$ in the core, as shown in Figure 10.

The zone affected by the free surface on two sides has a constant width C, in which the back-stress τ_b increases from 0 to $\tau^\dagger$ in a power law with the exponent of α. The length of the core is L-2C, in which the saturated back-stress τ_b is equal to $\tau^\dagger$. Then a general format for the relationship between the average back-stress $\overline{\tau}_b$ and the dislocation path length L can be summarized as Equation (7):

$$\overline{\tau}_b(L)=\frac{1}{L}\int_0^L \tau_b dl=\begin{cases}\dfrac{1}{\alpha+1}\left(\dfrac{L}{2C}\right)^{\alpha}\tau^\dagger & L<2C\\ \left(1-\dfrac{\alpha}{\alpha+1}\dfrac{2C}{L}\right)\tau^\dagger & L>2C\end{cases} \tag{7}$$

In particular, if the exponent α is 1 and the basic slip resistance τ^* is much smaller than the average back-stress $\overline{\tau}_b$, then for a specimen with short dislocation path ($L<2C$), the yield criterion Equation (6) in the tensile case can be rewritten as Equation (8). The effective $SF'_{\{111\}\langle101\rangle}$ in this case, can be replaced by L dependent $(4C/L)SF_{\{111\}\langle101\rangle}$ under Schmid's law, as reported by K. S. Raghavan[29] and T. L. Wu.[43]

$$\sigma^{YS}_{r+}\approx\frac{\overline{\tau}_b(L)}{SF_{\{111\}\langle101\rangle}}=\frac{\tau^\dagger}{(4C/L)SF_{\{111\}\langle101\rangle}}=\frac{\tau^\dagger}{SF'_{\{111\}\langle101\rangle}},\quad SF'_{\{111\}\langle101\rangle}=\frac{4C}{L}SF_{\{111\}\langle101\rangle} \tag{8}$$

And for a specimen with long dislocation path ($L>2C$), the average back-stress $\overline{\tau}_b$ presents a negative linear relationship with the reciprocal of dislocation path length L^{-1}. The $\overline{\tau}_b$ gradually approaches to the saturated value $\tau^\dagger$ and no longer presents L dependent if only the dislocation path is long enough.

In specific to the cases in this research under MT (600°C), the lengths L of dislocation paths are different between [010] and [110] transversely oriented rectangular-sectional specimens with the same thickness t, as shown in Figure 11. Therein the dislocation path

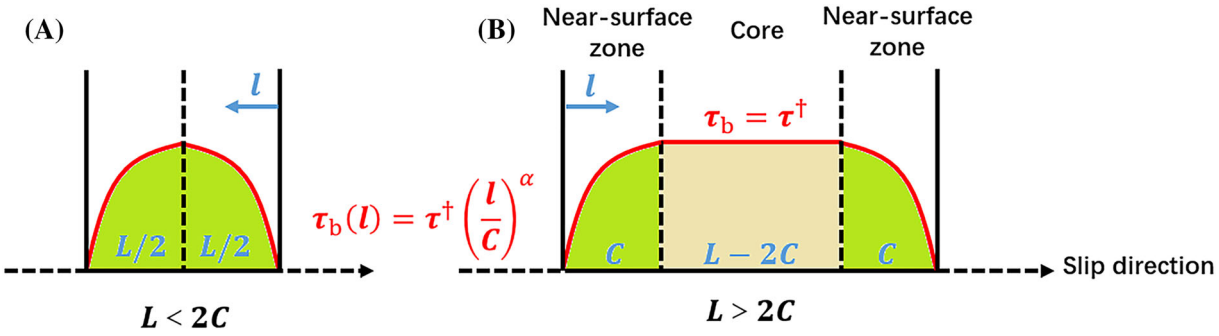

FIGURE 10 The back-stress τ_b distribution along the slip direction in specimens with (A) short and (B) long dislocation paths. [Colour figure can be viewed at wileyonlinelibrary.com]

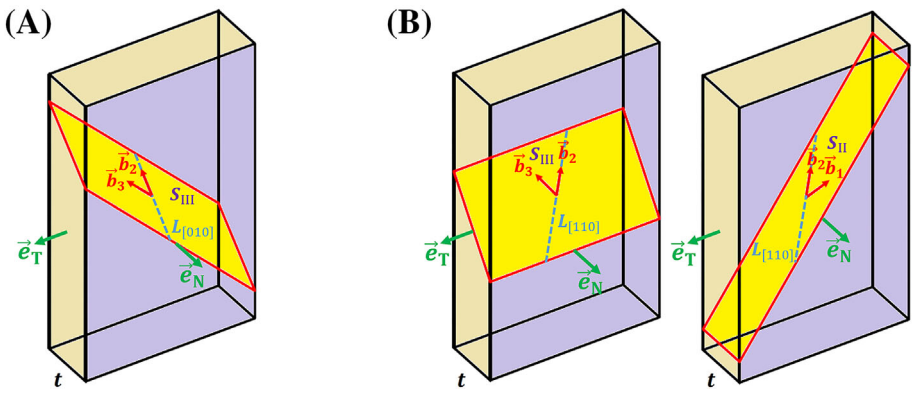

FIGURE 11 The length L of dislocation path moving along the slip direction across the thickness in (A) [010] and (B) [110] transversely oriented rectangular-sectional specimens. [Colour figure can be viewed at wileyonlinelibrary.com]

length can be calculated as $L = t/\left|\left(\vec{\boldsymbol{b}}_2/\left|\vec{\boldsymbol{b}}_2\right|\right)\cdot\vec{\boldsymbol{e}}_N\right|$, and the results are $L_{[110]} = 2t$ and $L_{[010]} = \sqrt{2}t$. The back-stress can be calculated by $\overline{\tau}_b = \left(\sigma^{YS}_{r+} - \sigma^{YS}_{r-}\right)\cdot SF_{\{111\}\langle 101\rangle}/2$, and the average results can be obtained from Table 3.

$$L_{[110]} : L_{[010]} = \sqrt{2} : 1,\ \overline{\tau}_b\left(L_{[110]}\right) : \overline{\tau}_b\left(L_{[010]}\right) = \frac{119+97+102}{3} : \frac{22+18+59}{3} \tag{9}$$

This relationship can be achieved if only the suitable parameters α and C are employed in the Equation (7).

With the increase of temperature from MT (600°C) to HT (850°C), NBSXs may no longer follow the yield criterion in Equation (6) due to the plastic deformation mechanism transition. Correspondingly, the tension-compression stress asymmetry also no longer presents secondary orientation dependent.

4.2 | Fatigue life difference between [010] and [110] transversely oriented specimens

Low cycle fatigue life difference between [010] and [110] transversely oriented rectangular-sectional specimens under MT (600°C) is another phenomenon worthy of being noticed. The conventional fatigue life prediction model for anisotropic NBSXs following the crystallographic fracture mode is the critical plane method,[21–27] where the activated {111} slip planes are usually defined as the critical plane[25] because the fatigue cracks nucleate along these crystallographic planes. Various critical plane parameters, such as Shear Strain Range (SSR) parameter,[21] Kandil parameter,[26] Chu-Conle-Bonnen (CCB) parameter,[27] and Findley parameter[28] and have been proposed by other researchers to serve as the indicators of low cycle fatigue damage on the critical planes. These parameters are the algebraic combinations of $\Delta\varepsilon^n$ (normal strain amplitude), $\Delta\gamma^t$ (shear strain amplitude), $\varepsilon^n{}_{max}$ (maximum normal strain), $\gamma^t{}_{max}$ (maximum shear strain), $\Delta\sigma^n$ (normal stress amplitude), $\Delta\tau^t$ (shear strain amplitude), $\sigma^n{}_{max}$ (maximum normal stress), and $\tau^t{}_{max}$ (maximum shear stress). Then the fatigue life can be then predicted by the power law: Kandil/CCB/Findley/SSR $= C(N_f)^n$. However, the critical plane method has the same problem as that of LCP model, i.e. it can only explain the dependence of low cycle fatigue life on the primary orientation but cannot explain the fatigue life difference induced by secondary orientation. All the items $\Delta\varepsilon^n/\Delta\gamma^t/\varepsilon^n{}_{max}/\gamma^t{}_{max}/\Delta\sigma^n/\Delta\tau^t/\sigma^n{}_{max}/\tau^t{}_{max}$ (i.e. the Kandil/CCB/Findley/SSR parameters) have already been determined once the primary orientation is fixed at [001], in which case N_f has nothing to do with the secondary orientation.

Therefore, the difference of low cycle fatigue life between [010] and [110] transversely oriented rectangular-sectional specimens should be attributed to the secondary orientation effect on the fatigue crack nucleation. It is known to all that the fatigue crack nucleation in NBSXs is achieved through the stress concentration near the micro notch accumulated by a lot of intrusions in the intersection between wall surface and PSB, as shown in Figure 12. The micro notch geometric size (depth: z, width: ω) is controlled by each single intrusion size (depth: h_b, width: w_n), which formed when two dislocations having the Burger's vector $\vec{\boldsymbol{b}}$ escaped from

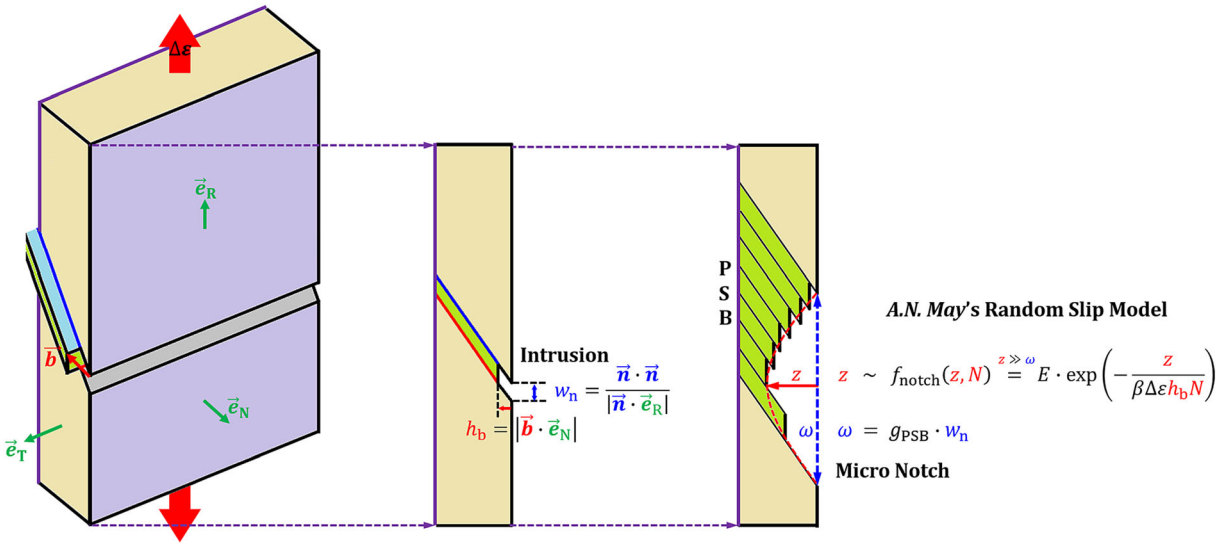

FIGURE 12 The formation of dislocation intrusion and micro notch by random slip on the wall surface. [Colour figure can be viewed at wileyonlinelibrary.com]

wall surface in pairs between the neighboring {111} slip planes. The intrusion's depth $h_b = \left|\vec{b}\cdot\vec{e}_N\right|$ is not always the same, which will be affected by the crystallographic orientation ([010] vs. [110]) along the normal direction $\vec{e}_N$ of the wall surface.

According to A.N. May's random slip model,[30,31] the fraction $f_{notch}(z, N)$ of those micro notches with width ω and depths between z and $z + dz$ after N cycles follows the evolution law shown in Equation (10), together with its approximate solution when $z \gg \omega$. The Burger's vector magnitude b in the original model is replaced by the intrusion's depth h_b here to consider secondary orientation effect.

$$\frac{\partial f_{notch}}{\partial N} = \left[\Delta\varepsilon h_b \omega\left(\alpha+\beta\frac{z}{\omega}\right)\right]\frac{\partial^2 f_{intru}}{\partial z^2},\ f_{notch}(z,N) \approx E \cdot \exp\left(-\frac{z}{\beta\Delta\varepsilon h_b N}\right) \tag{10}$$

On one hand, the critical depth Z_c of a micro notch with width ω which causes the stress concentration enough to nucleate a fatigue crack ($\Delta\sigma_c > \Delta\sigma_{th}$) can be calculated based on the stress concentration factor ($1 + M{\cdot}Z_c/\omega$) of a half-ellipse notch (half major axis: Z_c, minor axis: ω), as shown in Equation (11). The coefficient M is equal to 2 for a whole-ellipse notch far away from the surface, but a little smaller than 2 for a half-ellipse notch on the wall surface considering surface relaxation effect.

$$\Delta\sigma_c = \Delta\sigma\left(1+M\frac{Z_c}{\omega}\right) \approx \Delta\sigma M\frac{Z_c}{\omega} = \Delta\sigma_{th},\ Z_c = \frac{\omega\Delta\sigma_{th}}{M\Delta\sigma} \tag{11}$$

On the other hand, the fraction F ($z \geq Z_c$) of those micro notches deeper than critical depth Z_c after N cycles can be calculated according to the approximate solution of A.N. May's random slip model shown in Equation (10), and the fatigue crack is believed to nucleate in a certain probability when the fraction F attain the critical value F_c, in which case the cycles number N can be defined as the fatigue crack nucleation life N_f (occupy the major part of fatigue rupture life), as shown in Equation (12):

$$F(z \geq Z_c) = \int_{Z_c}^{\infty} f_{notch}(z, N_f)dz = \exp\left(-\frac{Z_c}{\beta\Delta\varepsilon h_b N_f}\right) = F_c,\ Z_c = \beta\Delta\varepsilon h_b N_f \ln(1/F_c) \tag{12}$$

Combining the critical depth Z_c and the critical fraction F_c of micro notches enough to nucleate a fatigue crack, we can obtain a power law between the strain amplitude $\Delta\varepsilon$ and the fatigue crack nucleation life N_f as shown in Equation (13), which is equivalent to the conventional Manson-Coffin's law.

$$\frac{\omega\Delta\sigma_{th}}{M\Delta\sigma} = \beta\Delta\varepsilon h_b N_f \ln(1/P_0),\ N_f\Delta\varepsilon\Delta\sigma = \frac{\omega\Delta\sigma_{th}}{M\beta h_b \ln(1/P_0)} = \frac{g_{PSB} w_n \Delta\sigma_{th}}{M\beta h_b \ln(1/F_c)} \tag{13}$$

Therein g_{PSB} is the average number of intrusions in each single PSB, h_b is the maximum depth of an intrusion formed by dislocations with the Burger's vector $\vec{b}$ escaping from the wall surface in pairs, and w_n is the width of an intrusion on the wall surface between neighboring {111} slip planes with the spacing vector $\vec{n}$. The intrusion's depth h_b and width w_n can be calculated as shown in Equation (14):

$$h_b = \max\left\{\left|\vec{b}_{1\sim4}\cdot\vec{e}_N\right|\right\} = \max\left\{\frac{a}{2}\sin\psi,\ \frac{a}{2}\cos\psi\right\},\ w_n = \frac{\vec{n}\cdot\vec{n}}{\left|\vec{n}\cdot\vec{e}_R\right|} = a \tag{14}$$

As mentioned before, the h_b is not always the same and is affected by the crystallographic orientation ([010] vs. [110]) along the normal direction ($\vec{e}_N$ or $\vec{e}_T$) of wall surface. Based on Equation (14), it can be derived that $h_b^{[010]} = a/2$, $h_b^{[110]} = \sqrt{2}a/4$ and $w_n^{[010]} = w_n^{[110]} = a$, and the fatigue life difference is essentially induced by the h_b difference between [010] and [110] cases. Combining the Equation (12) and the Equation (13), we can then make the conclusion that $N_f\Delta\varepsilon\Delta\sigma|^{[010]} = N_f\Delta\varepsilon\Delta\sigma|^{[110]}/\sqrt{2}$.

Figure 13 gives the unified S-N_f curves ($S = \Delta\varepsilon\Delta\sigma$) of different rectangular-sectional specimens ([010] vs. [110]) under MT (600°C), where the fatigue life of [110] transversely oriented rectangular-sectional specimen was modified by $\overline{N}_f^{[110]} = N_f^{[110]}/\sqrt{2}$. The data points (blue [010] vs. red [110]) under logarithmic coordinate become much closer to a single line after making the above modification.

With the increase of temperature from MT (600°C) to HT (850°C), NBSXs may no longer follow the A.N. May's random slip model due to the transitions of plastic deformation mechanism and fracture mode. Correspondingly, the fatigue life N_f also no longer depends on secondary orientation.

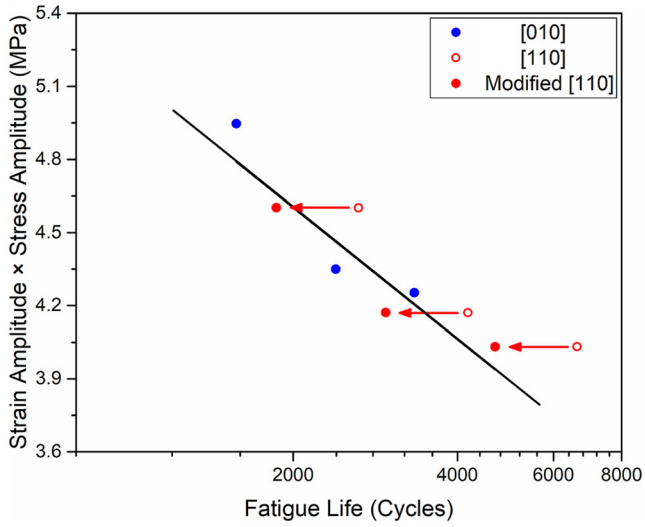

FIGURE 13 Unified S-N_f curves of different rectangular-sectional specimens with different secondary orientations ([010] vs. [110]) under 600°C. [Colour figure can be viewed at wileyonlinelibrary.com]

5 | CONCLUSIONS

The secondary orientation effects on the low cycle fatigue behaviors of rectangular-sectional NBSXs under MT (600°C) to HT (850°C) have been investigated. Through designing special rectangular-sectional specimens having different secondary orientations ([010] vs. [110]), as well as conducting the low cycle fatigue tests on these specimens under three strain amplitudes (± 0.63% / ± 0.66% / ± 0.69%) and two temperatures (600°C/850°C), several experimental results can be obtained by this research:

1. The tension-compression stress asymmetry difference between [010] and [110] transversely oriented rectangular-sectional specimens only existed under MT but disappeared under HT. In the former case, the stress ratio $R_\sigma^{[010]}$ is lower than $R_\sigma^{[110]}$ but similar to R_σ of the round bar specimen.
2. The low cycle fatigue life difference between [010] and [110] transversely oriented rectangular-sectional specimens also only existed under MT but disappeared under HT. In the former case, the fatigue life $N_f^{[010]}$ is shorter than $N_f^{[110]}$, and their relationship is $N_f\Delta\varepsilon\Delta\sigma\big|^{[010]} = N_f\Delta\varepsilon\Delta\sigma\big|^{[110]}/\sqrt{2}$.

Then this research discussed the causations of the above results and established suitable models:

3. With the temperature increase from MT to HT, the disappearance of secondary orientation effects on low cycle fatigue behaviors of rectangular-sectional NBSXs was attributed to the transitions of plastic deformation mechanism and fracture mode, which also accords with our previous research.
4. The conventional LCP model cannot explain the dependence of tension-compression stress asymmetry on secondary orientation, and therefore a back-stress model dependent on dislocation path length was employed, attributing different stress asymmetry to the different dislocation path lengths.
5. The conventional critical plane method also cannot explain the dependence of low cycle fatigue life on secondary orientation, and therefore an evolution law of micro notch controlled by A.N. May's random slip model for fatigue crack nucleation was proposed in this research, attributing different fatigue lives to the different depths of those intrusions induced by dislocations escaping from surface.

AUTHOR CONTRIBUTION

Shao-Shi Rui: Conceptualization; investigation; writing—original draft preparation. **Zhiwu He:** Methodology; data curation. **Yiyun Guo:** Formal analysis. **Yue Su:** Writing—review and editing. **Qi-Nan Han:** Resources. **Xianfeng Ma:** Data curation; methodology; supervision. **Hui-Ji Shi:** Funding acquisition.

ACKNOWLEDGEMENTS

This research work is financially supported by the National Natural Science Foundation of China (Nos. 12202446, U2032143, 12172193, 12002155, and 12102348), the National Major Science and Technology Projects of China (No. J2019-VI-0002-0115), the Opening Fund of Key Laboratory of Aero-engine Thermal Environment and Structure, Ministry of Industry and Information Technology (No. CEPE2022004), as well as the Opening Fund of State Key Laboratory of Nonlinear Mechanics. A deep sense of gratitude also goes to Prof. Yujie Wei, Prof. Qing Peng, and Prof. Chengqi Sun, for their meaningful discussions, kind encouragements, and unconditional supports to this research work.

DATA AVAILABILITY STATEMENT

The experimental data required to reproduce findings of this study cannot be shared online at this moment due to the time limitations, but are available from the corresponding authors upon request.

ORCID

Shao-Shi Rui https://orcid.org/0000-0002-9271-1322
Zhiwu He https://orcid.org/0000-0002-6244-4593
Yue Su https://orcid.org/0000-0001-8705-2783

REFERENCES

1. Reed RC. *The superalloys: fundamentals and applications*. Cambridge University Press; 2008.
2. Arakere NK, Swanson G. Effect of crystal orientation on Fatigue Failure of Single Crystal Nickel Base Turbine Blade Superalloys. Paper presented at: ASME Turbo Expo 2000: sssPower for Land, Sea, and Air 2000.
3. Segersäll M, Moverare J, Leidermark D, Simonsson K. Low-cycle fatigue behaviour of a Ni-based single-crystal superalloy. *Adv Mat Res*. 2014;891-892:416-421.
4. Ezz SS, Pope DP, Paidar V. The tension/compression flow stress asymmetry in Ni3(Al,Nb) single crystals. *Acta Metall*. 1982;30(5):921-926.
5. Takeuchi S, Kuramoto E. Temperature and orientation dependence of the yield stress in Ni3Ga single crystals. *Acta Metall*. 1973;21(4):415-425.
6. Pope DP, Ezz SS. Mechanical properties of Ni3AI and nickel-base alloys with high volume fraction of γ'. *Int Metal Rev*. 1984; 29(1):136-167.
7. Jiao F, Bettge D, Österle W, Ziebs J. Tension—compression asymmetry of the (001) single crystal nickel base superalloy SC16 under cyclic loading at elevated temperatures. *Acta Mater*. 1996;44(10):3933-3942.
8. Miner RV, Gabb TP, Gayda J, Hemker KJ. Orientation and temperature dependence of some mechanical properties of the single-crystal nickel-base superalloy René N4: part III. Tension-compression anisotropy. *Metall Trans a*. 1986;17(3): 507-512.
9. Gabb TP, Gayda J, Miner RV. Orientation and temperature dependence of some mechanical properties of the single-crystal nickel-base superalloy René N4: part II. Low cycle fatigue behavior. *Metall Trans a*. 1986;17(3):497-505.
10. Shah DM, Duhl DN. Paper presented at: superalloy 1984, American Institute of Mining, Metallurgical and Petroleum Engineers1984; Warrendale, PA, USA.
11. Qin Q, Bassani JL. Non-schmid yield behavior in single crystals. *J Mech Phys Solids*. 1992;40(4):813-833.
12. Paidar V, Pope DP, Vitek V. A theory of the anomalous yield behavior in L12 ordered alloys. *Acta Metall*. 1984;32(3):435-448.
13. Nabarro FRN. Extended dislocations and the schmid law of resolved shear stress. *Philos Mag a*. 1966;14(130):861-866.
14. Ma X, Shi H, Gu J, Wang Z, Harders H, Malow T. Temperature effect on low-cycle fatigue behavior of nickel-based single crystalline superalloy. *Acta Mech Solida Sin*. 2008;21(4): 289-297.
15. Lall C, Chin S, Pope DP. The orientation and temperature dependence of the yield stress of Ni3 (Al, Nb) single crystals. *Metall Trans a*. 1979;10(9):1323-1332.
16. Lukáš P, Kunz L, Svoboda M. High-temperature ultra-high cycle fatigue damage of notched single crystal superalloys at high mean stresses. *Int J Fatig*. 2005;27(10):1535-1540.
17. Zhang JH, Hu ZQ, Xu YB, Wang ZG. Dislocation structure in a single-crystal nickel-base superalloy during low cycle fatigue. *Metall Trans a*. 1992;23(4):1253-1258.
18. Décamps B, Brien V, Morton AJ. Deformation microstructures after low-cycle fatigue at 950°C in ni-based superalloys: the effect of test conditions. *Sc Metall Mater*. 1994;31(7):793-798.
19. Manson SS. Behavior of materials under conditions of thermal stress. *Tech Rep Arch Image Libr*. 1953;7(s 3–4):661-665.
20. Coffin LFJ. A study of the effects of cyclic thermal stresses on a ductile metal. *Ryūmachi [Rheumatism]*. 1953;22(6):419-606.
21. Naik RA, Deluca DP, Shah DM. Critical plane fatigue modeling and characterization of single crystal nickel superalloys. *J Eng Gas Turbine Power*. 2002;126(2):391-400.
22. Brown MW, Miller KJ. A theory for fatigue failure under multiaxial stress-strain conditions. *Proc Inst Mech Eng*. 1973;187(1): 745-755.
23. Fatemi A, Socie DF. A critical plane approach to multiaxial fatigue damage including out-of-phase loading. *Fract Eng Mater Struct*. 1988;11(3):149-165.
24. Chu C-C. Fatigue damage calculation using the critical plane approach. *J Eng Mater Tech*. 1995;117(1):41-49.
25. Leidermark D, Moverare J, Simonsson K, Sjöström S. A combined critical plane and critical distance approach for predicting fatigue crack initiation in notched single-crystal superalloy components. *Int J Fatig*. 2011;33(10):1351-1359.
26. Kandil FA, Brown MW, Miller KJ. *Biaxial low-cycle fatigue failure of 316 stainless steel at elevated temperatures*. Metals Society; 1982.
27. Chu C-C, Conle FA, Bonnen JJ. Multiaxial stress-strain modeling and fatigue life prediction of SAE axle shafts. *ASTM Spec Tech Publ*. 1993;1191:37-37.
28. Findley WN. A theory for the effect of mean stress on fatigue of metals under combined torsion and axial load or bending. *J Eng Ind*. 1959;81(4):301-305.
29. Raghavan KS, Kuhlmann-Wilsdorf D. Regarding the effect of specimen shape on the selection of the primary slip plane. *Mater Sci Eng a*. 1966;1(3):195-197.
30. May AN. A model of metal fatigue. *Nature*. 1960;185(4709): 303-304.
31. May AN. Random slip model of fatigue and Coffin's law. *Nature*. 1960;188(4750):573-574.
32. Guo Z, Fu T, Fu H. Crystal orientation measured by XRD and annotation of the butterfly diagram. *Mater Charact*. 2000;44(4): 431-434.
33. He Z, Zhang Y, Qiu W, Shi H-J, Gu J. Temperature effect on the low cycle fatigue behavior of a directionally solidified nickel-base superalloy. *Mater Sci Eng a*. 2016;676:246-252.
34. *Standard practice for strain-controlled fatigue testing*. ASTM International; 2004.
35. Schmid E. Paper presented at: Proceedings of the first International Congress for Applied Mechanics 1924; Delft, Netherlands.
36. Fourie J. The flow stress gradient between the surface and centre of deformed copper single crystals. *Philos Mag a J Theor Exper Appl Phys*. 1968;17(148):735-756.
37. Fourie JT. The plastic deformation of thin copper single crystals. II. An electron microscope study of the surface structure. *Can J Phys*. 1967;45(2):777-786.
38. Fourie JT. Plastic deformation of thin copper single crystals. I. The separate roles of edge and screw dislocations in stage I of work hardening. *Philos Mag a J Theor Exper Appl Phys Ther*. 1967;15(133):187-198.
39. Fourie JT. Sub-surface dislocation structure of deformed copper. *Philos Mag a J Theor Exper Appl Phys*. 1970;21(173): 977-985.
40. Mughrabi H. Electron microscope observations on the dislocation arrangement in deformed copper single crystals in the

stress-applied state. *Philos Mag a J Theor Exper Appl Phys*. 1968;18(156):1211-1217.

41. Mughrabi H. Investigations of plastically deformed copper single crystals in the stress-applied state. I. a study of the dislocation behaviour in the surface region and in the bulk. *Phys Status Solidi C*. 1970;39(1):317-327.
42. Mughrabi H. Some consequences of surface and size effects in plastically deformed copper single crystals. *Phys Stat Solidi (b)*. 1971;44(1):391-402.
43. Wu TL, Smoluchowski R. A new criterion for the occurrence of slip in thin single crystals. *Phys Rev*. 1950;78(4):468-469.

How to cite this article: Rui S-S, He Z, Guo Y, et al. Secondary orientation effects on the low cycle fatigue behaviors of rectangular-sectional Ni-based single crystal superalloys at medium and high temperatures. *Fatigue Fract Eng Mater Struct*. 2023; 46(9):3290-3305. doi:10.1111/ffe.14076